J. Fluid Mech. (1982), *vol.* 125, *pp.* 319–345
Printed in Great Britain

Observations of inertial waves in a homogeneous rotating fluid

By K. E. HEIKES AND T. MAXWORTHY
University of Southern California, Los Angeles, CA. 90007, U.S.A.

(Received 17 December 1981 and in revised form 25 May 1982)

Observations of inertial waves generated by uniform horizontal flow over ridges and truncated axisymmetric obstacles in a homogeneous fluid rotating about a vertical axis are discussed and compared with linear theory. The dependence of the flow on obstacle shape, Ro, H, E and ϵ is investigated. Here $Ro = U/2\Omega L$ is the Rossby number, $H = Ro(D/L)$, $E = \nu/2\Omega L^2$ is the Ekman number, and $\epsilon = h/L$ is the non-dimensional height of the obstacle, where U is the basic velocity, Ω is the angular frequency, L is a streamwise length, D is the depth of the fluid, h is the height of the obstacle, and ν is the kinematic viscosity. Previous linear analysis of this problem has been for the limit H fixed, $Ro \rightarrow 0$, referred to here as the small-Ro limit. However, it is shown that certain linear terms neglected in the small-Ro limit can be important for finite Ro, and are included in the analysis given here. The observed flow is then well described by linear theory for $H/\epsilon \gg 1$, particularly in the case of two-dimensional flow over a ridge. However, for $H/\epsilon \ll 1$ the flow field is dominated by a vertical columnar motion, which is not adequately described by the analysis.

1. Introduction

One of the most striking properties of slow steady relative motion in a rapidly rotating inviscid fluid is the tendency for the flow to be invariant in the direction parallel to the axis of rotation. This is a result of the primary balance between pressure gradient and Coriolis forces that leads to the well-known Proudman–Taylor theorem (Proudman 1916; Taylor 1917). Taylor (1923) demonstrated the implications of this balance in an experiment in which he slowly towed a truncated right-circular cylinder across the horizontal bottom of a tank rotating about a vertical axis. He found that fluid not only flowed around the cylinder but also flowed around a column of relatively stagnant fluid above the cylinder. This column is now commonly referred to as a Taylor column, a term suggested by Hide (1961), who based a model of Jupiter's Great Red Spot on this phenomenon. Subsequent work suggests that the stagnant column observed by Taylor forms only for Rossby numbers less than some critical value, where the critical value Ro_c depends on initial conditions, viscosity, fluid depth and obstacle height and shape (Jacobs 1964; Ingersoll 1969; Huppert 1975; Johnson 1978).

Another important property of rotating fluids is that even a homogeneous rotating fluid can support inertial waves. In fact it has been suggested the inertial waves are the more general property (Greenspan 1969, pp. 2, 3) and that the strong tendency towards two-dimensionality is only a manifestation of inertial wave propagation in the limit of zero excitation frequency. Lighthill (Hide, Ibbetson & Lighthill 1968; Lighthill 1970) considered the inertial wave field generated by a sphere moving with constant velocity normal to the rotation axis as a model for a Taylor column. He pointed out that the largest-amplitude inertial modes excited by flow over an obstacle are those with wavelengths comparable to the dimensions of the obstacle. He estimated that in the far field most of the energy is due to these modes and is confined to a narrow cone, the axis of which trails the obstacle and makes an angle ϕ with the axis of rotation, where

$$\phi = \arctan\,(\tfrac{3}{2}Ro).$$

Hide *et al.* (1968) found that the angle ϕ was in good agreement with that observed experimentally and called the trailing disturbance a 'tilted Taylor column', implying that the inertial waves and the Taylor column are one and the same phenomenon. However, on the basis of the present experiments and other recent work, this does not appear to be the case. It now seems clear that inertial waves are neither the primary cause of two-dimensionality nor are they responsible for the Taylor column, since, for example, they produce neither the vertically uniform nor the horizontally asymmetric motion characteristic of a Taylor column.

A partial explanation for the columnar appearance of the inertial wave disturbance observed by Hide *et al.* (1968) was provided by Mason & Sykes (1981) and Johnson (1982). They pointed out that short wavelengths are strongly damped by viscosity and do not appear in experimental observations. Therefore, the disturbance observed experimentally is mainly due to the long wavelengths whose surfaces of constant phase do not curve significantly near the obstacle, and, since further from the source their amplitude is negligible owing to damping and dispersion, the inertial wave disturbance has the form of a uniform tilted column near the obstacle.

Cheng, (1977) formulated far-field inertial-wave solutions for steady, inviscid, infinitely deep flow over a thin axisymmetric obstacle. He confirmed the phase structure of Lighthill's (Hide *et al.* 1968) solution and provided an explicit description of the far-field structure on obstacle shape. However, owing to an error in his far-field analysis, he predicted that the amplitude was undiminished downstream. Corrected results, along with numerical examples, have recently been presented by Cheng & Johnson (1982) and now agree in general with Lighthill with regard to decay downstream. Stewartson & Cheng (1979) show that in addition to obstacle shape, fluid depth plays an important role in determining the strength of the inertial waves. In an infinitely deep fluid the inertial-wave spectrum is continuous. However, when the depth is finite the modes are discretized and certain parts of the spectrum may be eliminated. In particular, as H decreases, the low-wavelength modes, which are, in general, the largest-amplitude modes, are eliminated and the contribution to the flow from the inertial waves becomes weaker. For this reason, caution must be exercised in ascribing the tilted columnar disturbance observed by Hide *et al.* (1968) in a relatively shallow fluid to the low-wavelength large-amplitude inertial-wave modes.

Stewartson & Cheng (1979) show that there exists an additional component of the flow field, distinct from the inertial waves, which resembles the flow around a Taylor column in that this component is vertically uniform, horizontally asymmetric and has no vertical velocity associated with it. The flow associated with this component is in agreement with that prescribed by the Proudman–Taylor theorem, and will be called the geostrophic component. Depth and obstacle thickness determine the strength of the geostrophic component because it is the result of vortex-tube compression, and the subsequent generation of relative vorticity, as fluid flows over the obstacle. The parameter which indicates the relative importance of the geostrophic component and inertial effects is H/ϵ, first used by Hide (1961). It has been shown by Huppert (1975), Johnson (1978) and Stewartson & Cheng (1979) that for $H/\epsilon \ll 1$ the geostrophic component prevails and closed streamlines appear above the obstacle, whereas, for $H/\epsilon \gg 1$, Stewartson & Cheng show that inertial effects dominate the flow.

The organization of this paper is as follows: In §2 we extend the inertial-wave solution of Stewartson & Cheng (1979) to finite *Ro* for linear steady inviscid flow over two-dimensional ridges of two basic shapes in a fluid of finite depth. Section 3 contains a description of the apparatus and the flow-visualization technique. In §4 we report the results of an experimental study of inertial waves generated by flow past an obstacle in a rapidly rotating fluid. Streamlines based on the solutions formulated in §2 are compared with observed wave patterns. The transition from a flow in which inertial waves are the predominant form of motion to one in which the geostrophic component prevails is briefly discussed.

2. The inertial waves

This analysis is mainly concerned with solutions to the linear steady inviscid two-dimensional equations, but the full nonlinear governing equations are developed to indicate the degree of validity of the linear approximation. Some linear asymptotic three-dimensional solutions are also discussed. Following Stewartson & Cheng (1979) we introduce the following scalings:

$$(x,\ y,\ z)^* = L\left(x,\ y,\ \frac{H}{Ro}z\right),\quad t^* = \frac{L}{U}t,$$

$$(u,\ v,\ w)^* = U(u,\ v,\ w),\quad p^* - p^*_e = 2\Omega UL\rho p,$$

where * denotes dimensional qualities. $p^* - p^*_e$ is the pressure deviation from its equilibrium value p^*_e. The coordinate system is Cartesian and attached to the moving obstacle in the rotating reference frame (figure 1). Horizontal lengths are scaled with one-half the streamwise length L of the obstacle, vertical lengths are scaled with the fluid depth D, the three components of velocity are scaled with the mean flow speed, U, and time is scaled with the advection time, L/U. The scaling for pressure reflects the basic geostrophic balance. The velocity and pressure fields are separated into geostrophic mean flow and perturbation components, and the perturbation components are rescaled to reflect the magnitude of the disturbance produced by an obstacle of non-dimensional height ϵ, i.e.

$$u = (1 + \epsilon u'),\quad v = \epsilon v',\quad w = \epsilon w',\quad p = -y + \epsilon p',$$

where $\epsilon = h/L$. The primes denote perturbation components. Dropping the primes, the governing equations become

$$u = -\frac{\partial p}{\partial y} - Ro\left[\frac{\partial}{\partial t} + \frac{\partial}{\partial x} + \epsilon\mathbf{u}\,.\,\nabla - \frac{E}{Ro}\nabla^2\right]v, \tag{2.1a}$$

$$v = \frac{\partial p}{\partial x} + Ro\left[\frac{\partial}{\partial t} + \frac{\partial}{\partial x} + \epsilon\mathbf{u}\,.\,\nabla - \frac{E}{Ro}\nabla^2\right]u, \tag{2.1b}$$

$$\frac{\partial p}{\partial z} = -H\left[\frac{\partial}{\partial t} + \frac{\partial}{\partial x} + \epsilon\mathbf{u}\,.\,\nabla - \frac{E}{Ro}\nabla^2\right]w, \tag{2.1c}$$

$$\nabla\,.\,\mathbf{u} = 0 \tag{2.1d}$$

where $$\nabla = \mathbf{i}\frac{\partial}{\partial x} + \mathbf{j}\frac{\partial}{\partial y} + \mathbf{k}\frac{Ro}{H}\frac{\partial}{\partial z},\quad \nabla^2 = \frac{\partial^2}{\partial x^2} + \frac{\partial^2}{\partial y^2} + \frac{Ro^2}{H^2}\frac{\partial^2}{\partial z^2}.$$

For reference we repeat the definitions

$$Ro = \frac{U}{2\Omega L},\quad H = Ro\frac{D}{L},\quad E = \frac{\nu}{2\Omega L^2},\quad \epsilon = \frac{h}{L}.$$

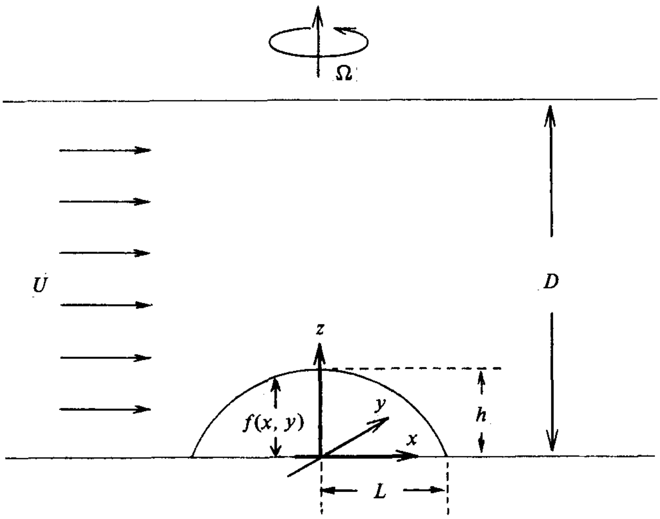

FIGURE 1. Cartesian coordinate system attached to the moving obstacle in the rotating reference frame.

The boundary conditions are

$$w = (1+\epsilon u)\frac{\partial f}{\partial x} + \epsilon v\frac{\partial f}{\partial y} \quad \text{at} \quad z = \epsilon\frac{Ro}{H}f(x, y), \tag{2.2a}$$

$$w = 0 \quad \text{at} \quad z = 1, \tag{2.2b}$$

where $f(x, y)$ defines the shape of the lower boundary (figure 1).

Combining the divergence and vertical component of the curl of (2.1) yields

$$\frac{\partial w}{\partial z} = H\left\{\left[\frac{\partial}{\partial t} + \frac{\partial}{\partial x} + \epsilon \mathbf{u}\,.\,\nabla - \frac{E}{Ro}\nabla^2\right](\nabla^2 p - Ro\epsilon\omega^2) - \epsilon\boldsymbol{\omega}\,.\,\nabla w\right\}, \tag{2.3}$$

where the vorticity vector is given by

$$\boldsymbol{\omega} = \mathbf{i}\left(\frac{\partial w}{\partial y} - \frac{Ro}{H}\frac{\partial v}{\partial z}\right) + \mathbf{j}\left(\frac{Ro}{H}\frac{\partial u}{\partial z} - \frac{\partial w}{\partial x}\right) + \mathbf{k}\left(\frac{\partial v}{\partial x} - \frac{\partial u}{\partial y}\right),$$

$$\omega^2 = \boldsymbol{\omega}\,.\,\boldsymbol{\omega}.$$

Note that $\boldsymbol{\omega}\,.\,\nabla w$ is $O(Ro/H)$.

We now approximate the governing equations and boundary conditions by the corresponding linear forms. Assuming that w and p are of unit order, to leading order

$$u = -\frac{\partial p}{\partial y} + O(Ro),$$

$$v = \frac{\partial p}{\partial x} + O(Ro).$$

For $Ro < H$, the nonlinear terms in (2.1c) and (2.3) may be neglected for $\epsilon H \ll 1$. However, as pointed out by Johnson (1982), the condition for linearization is less stringent in the two-dimensional case where $\partial/\partial y = 0$ and therefore $u \sim O(Ro)$. Thus, the nonlinear terms in (2.1c) and (2.3) may be neglected for $\epsilon H Ro \ll 1$, or $\epsilon Ro \ll 1$ for $H < 1$. In addition to approximating (2.1c) and (2.3) by their linear forms, previous studies (Hide *et al.* 1968; Cheng 1977; Stewartson & Cheng 1979; Johnson 1982) have used the limit H fixed, $Ro \to 0$, which will be referred to as the small Ro limit. In this limit the second-order partial derivative with respect to z, $(Ro/H)^2\, \partial^2/\partial z^2$, in the Laplacian operator is neglected. Here this term is retained and will be shown to be possibly as large or larger than the derivatives with respect to x and y in the Laplacian. Therefore it is not inconsistent to retain this term while neglecting nonlinear terms that at first appear to be larger. Proceeding to linearize (2.1c) and (2.3),

$$\frac{\partial p}{\partial z} = -H\left[\frac{\partial}{\partial t} + \frac{\partial}{\partial x} - \frac{E}{Ro}\nabla^2\right] w, \tag{2.4a}$$

$$\frac{\partial w}{\partial z} = H\left[\frac{\partial}{\partial t} + \frac{\partial}{\partial x} - \frac{E}{Ro}\nabla^2\right] \nabla^2 p. \tag{2.4b}$$

Equations (2.4a, b) combine to yield a single equation in either w or p:

$$\left\{H\left[\frac{\partial}{\partial t} + \frac{\partial}{\partial x} - \frac{E}{Ro}\nabla^2\right]^2 \nabla^2 \frac{\partial^2}{\partial z^2}\right\} w,\, p = 0. \tag{2.5}$$

The boundary condition (2.2a) on w at $z = (\epsilon Ro/H) f(x, y)$ can be approximated by a boundary condition on w at $z = 0$ with an error $O(\epsilon Ro/H)$. Linearization is valid for $\epsilon \ll 1$ in the three-dimensional case or $\epsilon Ro \ll 1$ in the two-dimensional case. The linear boundary conditions are

$$w(x, y, 0) = \frac{\partial f}{\partial x}, \tag{2.6a}$$

$$w(x, y, 1) = 0. \tag{2.6b}$$

Assuming solutions of the form $A(\mathbf{k}, \sigma) \exp(i\mathbf{k}\,.\,\mathbf{x} + \sigma t)$, where

$$\mathbf{k} = (k_x, k_y, (Ro/H)\, k_z) \quad \text{and} \quad \mathbf{x} = (x, y, (H/Ro)\, z),$$

the dispersion relation corresponding to (2.5) is

$$\sigma = -i\left(k_x \pm \frac{k_z}{Hk}\right) - \frac{E}{Ro} k^2, \tag{2.7}$$

where $k = |\mathbf{k}|$. Equation (2.7) shows that viscous damping is proportional to the square of the wavenumber. Thus short waves are more strongly damped than long waves.

We now restrict our attention to steady inviscid flows. The neglect of viscosity is valid for $E^{\frac{1}{2}} \ll H$ and $E \ll HRo$ (Stewartson & Cheng, 1979), which holds in most of the experimental cases considered here. For steady, inviscid flow (2.7) reduces to

$$k_z = \pm \frac{Hk_x (k_x^2 + k_y^2)^{\frac{1}{2}}}{(1 - Ro^2 k_x^2)^{\frac{1}{2}}}. \tag{2.8}$$

It is now clear that differentiation with respect to z in the Laplacian operator can give rise to terms as large as those resulting from differentiation with respect to x and y. Substituting for k_z from (2.8), the ratio of the vertical and horizontal components in the Laplacian operator is

$$\frac{Ro^2 k_x^2}{1 - Ro^2 k_x^2}.$$

Thus, if terms resulting from differentiation with respect to z cannot be neglected when they are at least one quarter as large as those resulting from differentiation with respect to x and y, then neglect of the vertical component of the Laplacian operator, as in the small-*Ro* approximation, is not valid for $Ro\,k_x \gtrsim 5^{-\frac{1}{2}}$. Thus the small-*Ro* approximation does not hold for wavelengths less than about $2\pi\, Ro\, 5^{\frac{1}{2}}$.

The general solution to (2.5) for a two-dimensional ridge of arbitrary shape is (Stewartson & Cheng 1979)

$$w(x,\, z) = \frac{1}{2\pi}\int_{-\infty}^{\infty} e^{ik_x x} F(k_x) \frac{\sin\left[k_z(1-z)\right]}{\sin k_z}\, dk_x, \tag{2.9}$$

where $F(k_x)$ is a weight function that ensures that $w(x,\, 0)$ satisfies (2.6*a*), i.e.

$$F(k_x) = ik_x \int_{-1}^{1} e^{-ik_x x} f(x)\, dx. \tag{2.10}$$

The integral (2.9) is evaluated by completing the contour with a semicircle, with closure above the real axis if $x+1 > 0$ and below if $x+1 < 0$, determined by the requirement that the contributions from the k_n^+ poles, defined below, decay exponentially. The solution is obtained by summing the contributions from the residues corresponding to the zeros of $\sin k_z$ and the poles of $F(k_x)$. The result is a slowly converging, infinite series. Convergence is accelerated by averaging successive partial sums (Fejer's method) but still requires summation over about 1000 terms for convergence at each point in the fluid. Convergence is slowest for large values of *Ro* or *H*.

The zeros of $\sin k_z$ that contribute residues to (2.9) occur for k_z real and equal to $n\pi$, $n = 1, 2, 3, \ldots$. Therefore, from (2.8), $k_x = \pm k_n^-$, $\pm ik_n^+$, where

$$k_n^- = \left\{\left[\left(\frac{n\pi}{\surd 2}\frac{Ro}{H}\right)^4 + \left(\frac{n\pi}{H}\right)^2\right]^{\frac{1}{2}} - \left(\frac{n\pi}{\surd 2}\frac{Ro}{H}\right)^2\right\}^{\frac{1}{2}}, \tag{2.11a}$$

$$k_n^+ = \left\{\left[\left(\frac{n\pi}{\surd 2}\frac{Ro}{H}\right)^4 + \left(\frac{n\pi}{H}\right)^2\right]^{\frac{1}{2}} + \left(\frac{n\pi}{\surd 2}\frac{Ro}{H}\right)^2\right\}^{\frac{1}{2}}. \tag{2.11b}$$

Equation (2.11*a*) shows that the wavenumbers k_n^- are limited to

$$k_n^- < Ro^{-1}. \tag{2.12}$$

as $n \rightarrow \infty$. This fundamental cutoff criterion is not obvious in the small-*Ro* limit, where $k_n = k_n^- = k_n^+ = (n\pi/H)^{\frac{1}{2}}$, and, therefore, $k_n \rightarrow \infty$ as $n \rightarrow \infty$ for fixed H. Equation (2.12) is just the steady non-dimensional version of the more-general dimensional cutoff condition on the Doppler-shifted frequency of an oscillatory source $\sigma^* + Uk_x^* < 2\Omega$ relating the frequencies of the waves in a translating reference frame to those in the stationary (rotating) reference frame when $\sigma^* = 0$. There is no cutoff wavenumber for the decaying modes k_n^+.

Streamlines calculated from the solution (2.9) provide a means for detailed comparison between calculations, which take into account the shape of the obstacle and the depth of the fluid, and experimental observations. These are given by

$$z(x) = z(-\infty) + \epsilon \frac{Ro}{H} \int_{-\infty}^{x} w(x,\, z(-\infty))\, dx. \tag{2.13}$$

Here terms $O(\epsilon^2 Ro^2/H)$ have been neglected in the two-dimensional case.

Another method used to compare experimental observations to theory is based on the asymptotic theory for linear dispersive waves in the far field developed by Lighthill (1960, 1965, 1967). Lighthill (1978) shows that in a system governed by linear equations with constant coefficients where there is no transfer of energy between waves, waves of wavevector **k** are found along the group path for that wavevector and have an amplitude proportional to $|F(\mathbf{k})|$. Therefore, regions of maximum and minimum amplitude within a wave pattern are determined by the positions of the group paths for the maximum- and minimum-amplitude wavevectors. It is possible to identify the group paths for wavevectors corresponding to zeros of $F(\mathbf{k})$ since no waves appear along these paths. These group paths are visible as quiescent regions within the wave pattern. The position of the observed quiescent region can then be compared with that calculated for the group path for the wavevector $\mathbf{k}_0$, where $F(\mathbf{k}_0) = 0$.

The group path for a wavevector **k** in the far field depends on *Ro*, and can be determined from the far-field group velocity with components

$$C_x = 1 + k_x^2 \frac{1 - Ro^2 k_x^2}{k_x^2 + k_y^2}, \tag{2.14a}$$

$$C_y = k_x\, k_y \frac{1 - Ro^2 k_x^2}{k_x^2 + k_y^2}, \tag{2.14b}$$

$$C_z = \frac{(1 - Ro^2 k_x^2)^{\frac{3}{2}}}{Ro(k_x^2 + k_y^2)^{\frac{1}{2}}}. \tag{2.14c}$$

Note that z^* is scaled with L rather than D in (2.14)–(2.16), so that the spatial coordinates are scaled uniformly to facilitate comparison of calculated and observed group paths and phase surfaces. Also, in (2.14)–(2.16) the small *Ro* limit is obtained by setting the $Ro^2 k_x^2$ terms equal to zero. For a wavevector **k** in the plane $y = 0$, subsequently referred to as the centre plane, (2.14*a*–*c*) show that the group path lies along a straight line sloping downstream at an angle ϕ from the z-axis, where

$$\phi = \arctan \frac{Ro\, k_x(2 - Ro^2 k_x^2)}{(1 - Ro^2 k_x^2)^{\frac{3}{2}}}. \tag{2.15}$$

For group paths sloping progressively downstream, (2.15) shows that the wavenumber increases as ϕ increases and that the cutoff wavenumber k_x corresponds to the horizontally directed group path $\phi = 90°$.

The forms of $F(k_x)$ for the two ridge shapes used in the experiment (defined in §3) are plotted in figure 2. The first zeros occur for $k_x = 4{\cdot}20$ for the cylindrical ridge and $k_x = \pi$ for the top-hat ridge. The group-path angles for the wavenumbers corresponding to the first zeros of $F(k_x)$ for the cylindrical ridge and $F(k_x, 0)$ for the spherical cap, $k_x = 4{\cdot}20$ and $4{\cdot}87$ respectively, are calculated and compared with experimental observations in §4. Assuming that the small-*Ro* limit does not hold for $Ro\, k_x \gtrsim 5^{-\frac{1}{2}}$, the group-path angles calculated for $k_x = 4.20$ and 4.87 based on the small-*Ro* limit are expected to be significantly in error for $Ro > 0{\cdot}11$ and $0{\cdot}09$ respectively.

The wave pattern is effected in other ways by the values of *Ro* and *H*. Figure 2 shows that the largest-amplitude modes are those with wavelengths comparable to $4L$, that is $k_x = \frac{1}{2}\pi$. For 'streamlined' ridges, such as the cylindrical ridge, $|F(k_x)|$ decreases as k_x increases. However, this it not true for ridges with sharp corners such as the top-hat ridge. Nevertheless, if *Ro* is large ($Ro > 1/\pi$), the high wavenumbers are not excited because of the cutoff condition, and there is little difference between the wavenumber spectra for blunt or smooth ridges. The vertical lines modulated by $|F_1(k_x)|$ in figure 2 are the values of k_n^- from (2.11*a*) plotted for $Ro = 0{\cdot}1$ and $H = 10$ in figure 2(*a*), and plotted for $Ro = 0{\cdot}1$ and $H = 1$ in figure 2(*b*). Figure

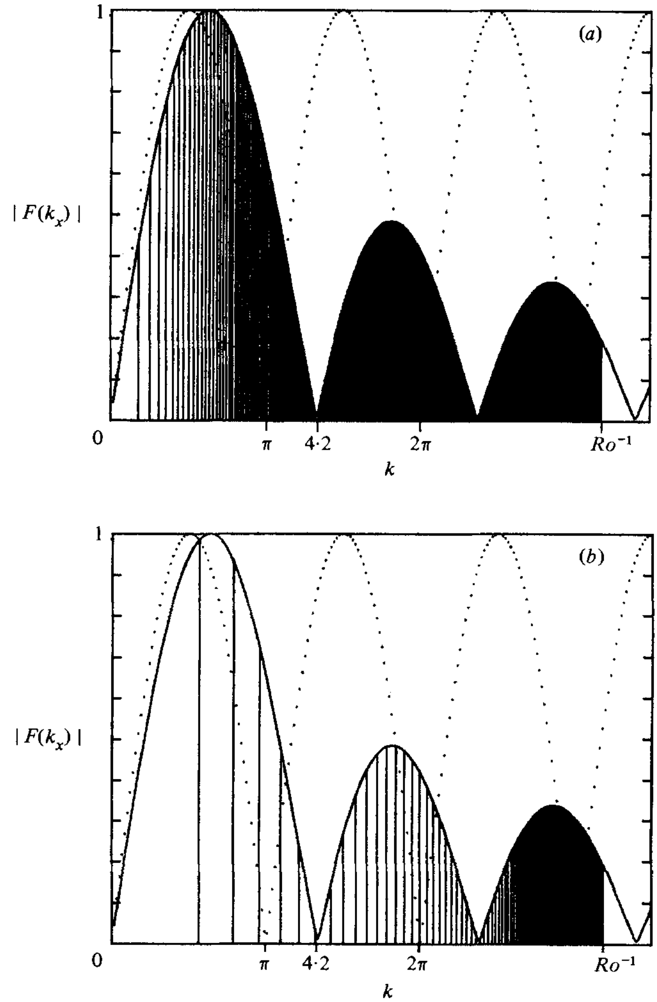

FIGURE 2. Normalized Fourier transforms, $|F_1(k_x)|/|F_{1\max}|$ and $|F_2(k_x)|/|F_{2\max}|$, of $\partial f_i/\partial x$ for the cylindrical ridge $f_1(x)$ (solid) and the top-hat ridge $f_2(x)$ (dotted) respectively. Vertical lines denote $|F_1(k_x)|/|F_{1\max}|$ for k_n^-, $n = 1,2,3,\ldots$, for (a) $Ro = 0{\cdot}1$, $H = 10$ and (b) $Ro = 0{\cdot}1$, $H = 1$.

2 shows that as H decreases, the largest-amplitude modes are eliminated. A similar trend for the low wavenumbers is obtained by fixing H and decreasing Ro. This suggests that for small Ro, in a fluid of finite depth, or for small H, the inertial waves are weak, as shown by Stewartson & Cheng (1979).

Qualitative comparisons are made of observed three-dimensional surfaces of constant phase and those predicted by Lighthill's theory. The far-field, three-dimensional surfaces of constant phase, are given in parametric form by

$$x = \frac{\Phi}{k_x}\left[1 + k_x^2 \frac{1 - Ro^2 k_x^2}{k_x^2 + k_y^2}\right], \tag{2.16a}$$

$$y = \Phi k_y \frac{1 - Ro^2 k_x^2}{k_x^2 + k_y^2}, \tag{2.16b}$$

$$z = \pm \frac{\Phi}{Ro\, k_x} \frac{(1 - Ro^2 k_x^2)^{\frac{3}{2}}}{(k_x^2 + k_y^2)^{\frac{1}{2}}}, \tag{2.16c}$$

where $\Phi = \Phi_0 + 2\pi n$, $n = 1, 2, 3, \ldots$, is a phase constant. Equation (2.16) shows that the lee waves from a point source are contained by a caustic or wave envelope with roughly the shape of a ship's bow. At $z = 0$ the caustic is a line training downstream from the source. As z increases, the caustic in horizontal planes becomes wedge-shaped, approaching 19·5° from the x-axis at the vertex of the wedge directly above the source and then curving downstream. In the small-*Ro* limit, the caustic lines are straight and meet at an angle of 19·5° from the x-axis in every horizontal plane.

Returning to the question of inclusion of the vertical derivative in the Laplacian operator, and taking into account (2.12), we see that this term must be included for $5^{-\frac{1}{2}} < Ro\, k_x < 1$. However, in applying this analysis to experimental results it is noted that the modes $k_x \approx Ro^{-1}$ contribute very little. The reason is that, first, the amplitudes of the short waves are small compared with those with wavelengths comparable to the streamwise body dimension, except for obstacles with sharp corners such as a top-hat ridge (figure 2), and, secondly, as indicated by (2.7), short wavelengths are strongly damped by viscosity. Nevertheless, it is observed that there does exist a range of k_x for $Ro\, k_x \geqslant 5^{-\frac{1}{2}}$ with amplitudes sufficiently large and undamped such that inclusion of the z-derivatives in the Laplacian operator provides significantly better agreement with experimental results than does the small-*Ro* limit.

In order to produce waves with amplitudes large enough to be detected visually, it is necessary to use relatively thick obstacles. In all the results discussed in §4, $\epsilon = 0{\cdot}61$. Owing to this large value of ϵ, and taking into account the maximum values of *Ro* and *H* used in the experiment, linearization is usually valid in the two-dimensional case, but the condition for linearization in the three-dimensional case, $\epsilon H \ll 1$, is often not met. Aside from discrepancies due to use of a linear approximation, discrepancies between observations and calculations may arise in several other ways. The two-dimensional calculations do not take into account the side-walls in (2.13), nor do they include the effect of finite depth in (2.15) and (2.16). In addition (2.15) and (2.16) are asymptotic descriptions of the waves far from the source and may not be good approximations relatively near the source. In spite of this, these calculations do provide a reasonably clear interpretation of certain visible features, and, moreover, are often in good agreement with observations.

3. Apparatus

Side- and plan-view schematic diagrams of the apparatus are shown in figure 3. The $0{\cdot}46 \times 0{\cdot}91 \times 1{\cdot}52$ m^3 acrylic tank (A) and its steel reinforcement and support frame (B) are mounted on a rotating turntable (C), which is driven by an electric motor (D). The obstacle (E) and traverse (F) are towed by means of a 0·79 mm stainless-steel cable powered by an electric motor (G). An aluminium box (H) is mounted on top of the acrylic tank. Guards (I) (the one on the left is hidden in the schematic) prevent water from spilling over the box during rotation. This box is open on top and closed on the bottom except for a 0·64 × 152 cm slit opening into the interior of the acrylic tank. Lights (J) shine through this slit and illuminate aluminium particles that are used to visualize the fluid motion. A switch (K) is mounted on the traverse and is activated by pegs (L) mounted on a bar (M) to trigger the camera as the obstacle and traverse, which move with the same velocity, are towed across the tank. The mirror (N), inclined at 45° from horizontal, is used to take photographs from beneath the tank. Slip rings (O) supply power to the rotating frame. The entire apparatus is levelled using the screws (P). The recording camera, which is not shown, can be mounted at various heights on the rotating table or the traverse to take photographs through the side or the bottom of the tank. When light is shone through the slit in

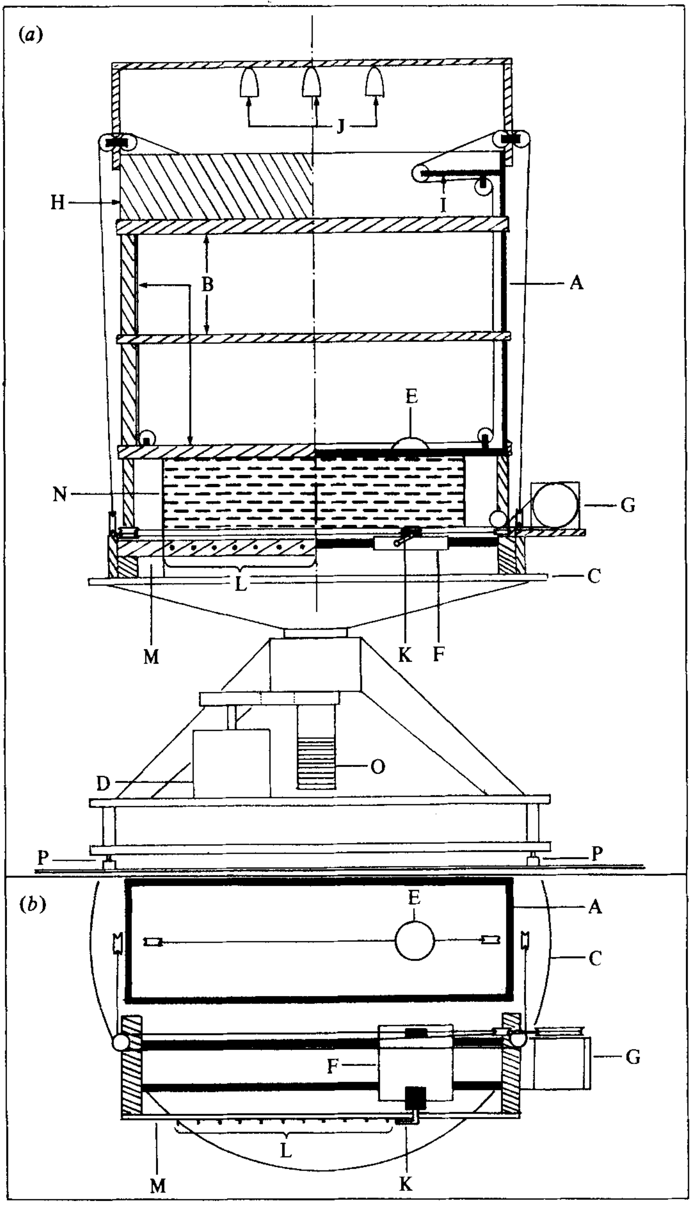

FIGURE 3. Schematic diagram of the experimental apparatus. (*a*) Side view. (*b*) Top view of the apparatus between the bottom of the tank and the top of the turntable.

the bottom of the box on top of the tank the centreplane is illuminated. When light is shone through slits at various heights on the side of the tank horizontal planes are illuminated.

The flow is made visible by a suspension of about 1 part aluminium powder to 10^5 parts water. The aluminium particles have the form of tiny plates. This technique makes use of the tendency for the axis normal to the plate to be aligned perpendicular to the local velocity gradient (Maxworthy 1971). When these particles are suitably oriented relative to the light source and the observer by velocity gradients in the fluid, light is reflected toward the observer, and regions of the fluid with that velocity gradient appear brighter than surrounding regions. Flakes in regions without appreciable shear are randomly oriented and the region has a uniform matté appearance. In flows, such as the one reported here, where accelerations and particle inertia are small, the particles follow the local translational motions of the fluid. Therefore streaks visible in time exposures of the flow correspond to fluid streaklines. Unfortunately, the length of these streaks does not provide a reliable measure of velocity because, although the majority of the flakes have a particular orientation, individual flakes are continually rotating and therefore a given particle may not reflect light toward the observer during the entire time exposure. However, the length of streaklines does at least give an indication of regions of high and low velocity.

This visualization technique is sensitive to relatively weak disturbances, and considerable care was required to avoid convection caused by heat from the lights and temperature differences between the fluid and the laboratory, which would otherwise obscure features of the flow being studied. Surprisingly, even the towing wire for the obstacle produced a visible disturbance over 150 towing-wire diameters away (see figures 10 and 12).

Two obstacle shapes were used in the experiment: one smooth and one with sharp corners. Each of these shapes was tested in both a two-dimensional and three-dimensional configuration. The three-dimensional forms have the same cross-sectional geometries in the plane $y = 0$ as their two-dimensional counterparts, but are axisymmetric about the vertical axis. The two cross-sectional shapes are

$$\begin{aligned} f_1(r) &= \epsilon^{-1}\{[(\tfrac{9}{8})^2 - r^2]^{\frac{1}{2}} - (\tfrac{17}{64})^{\frac{1}{2}}\} \quad (r < 1) \\ &= 0 \quad (r \geqslant 1), \\ f_2(r) &= 1 \quad (r < 1) \\ &= 0 \quad (r \geqslant 1), \end{aligned}$$

where $\epsilon = \frac{9}{8} - (\frac{17}{64})^{\frac{1}{2}} = 0{\cdot}6096$. The first shape f_1 generates a ridge that is a section of a cylinder or a hemispherical cap. The second shape f_2 generates a top-hat ridge or a truncated right-circular cylinder.

The effective depth of the tank was varied by changing the size of the obstacle or the depth itself. The depths used were $D = 22{\cdot}9$, $45{\cdot}7$ and $91{\cdot}4$ cm. Obstacle radii, or values of half the streamwise length, used in the experiment were $L = 1{\cdot}27, 2{\cdot}54, 3{\cdot}81, 5{\cdot}08$ and $10{\cdot}16$ cm. The angular frequencies used were $\Omega = 1{\cdot}00$, $2{\cdot}00$, and $4{\cdot}00$ s^{-1}. The towing speed was varied continuously from $U = 0{\cdot}043$ to $2{\cdot}64$ cm/s. This allowed the following ranges of parameters; $0{\cdot}0005 < Ro < 1{\cdot}04$, $0{\cdot}0012 < H < 74{\cdot}9$, $0{\cdot}11 \times 10^{-4} < E < 28{\cdot}3 \times 10^{-4}$. However, these parameters could not be varied independently within these ranges.

4. Results

For each series of observations we have tried to run the experiment long enough that all transients have disappeared. In practice the time available for observations is limited to the length of time for the obstacle to traverse the tank and the time before internal wave reflections within the tank significantly modify waves within the region of observation. However, this is not a severe restriction, and the observations presented here are probably indistinguishable from the steady-state wave pattern.

Streamlines have been calculated from (2.13) for $f_3(x) = 1 - 0{\cdot}646x^2 - 0{\cdot}354x^4$ for

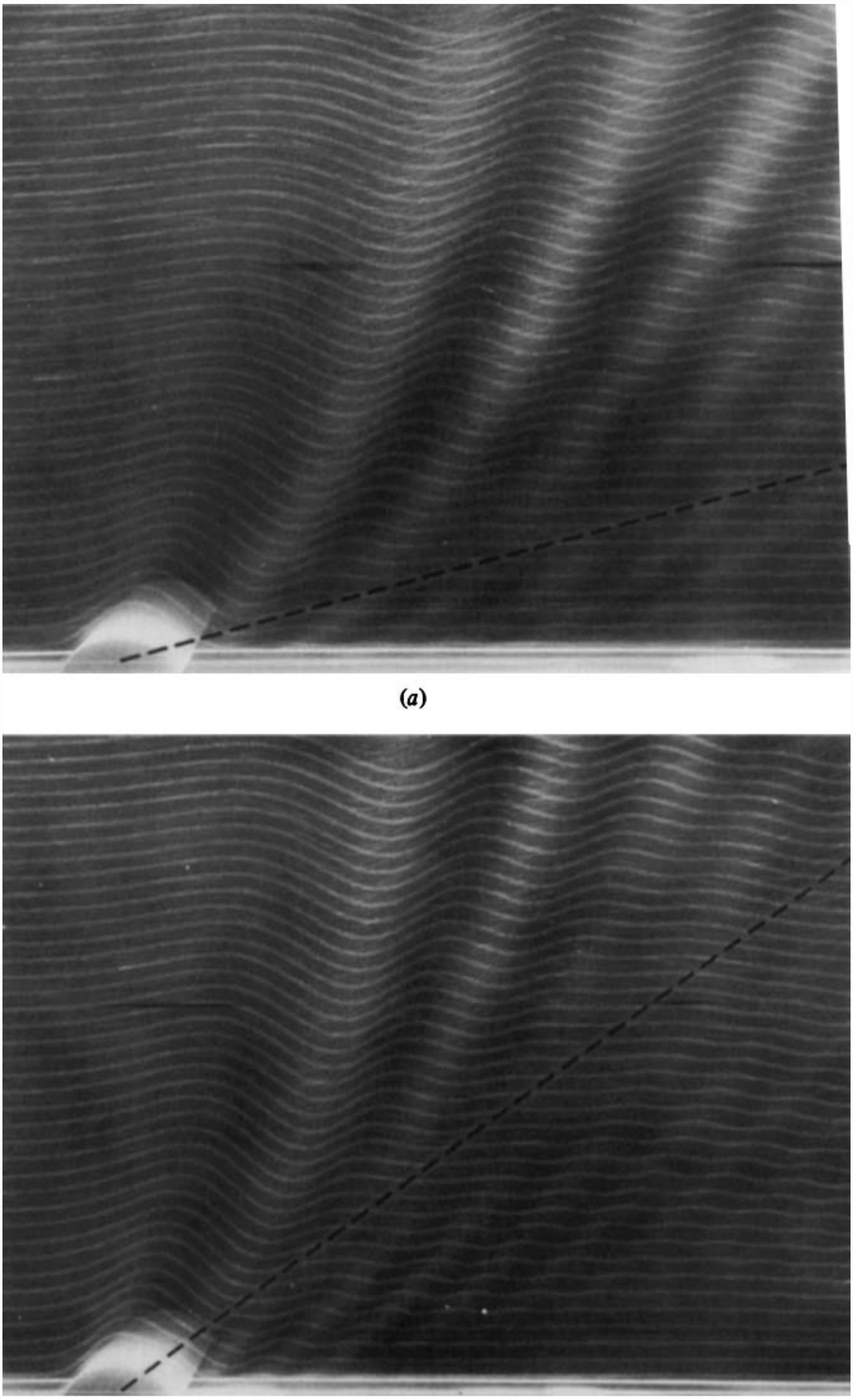

FIGURE 4 (a, b). For caption see facing page.

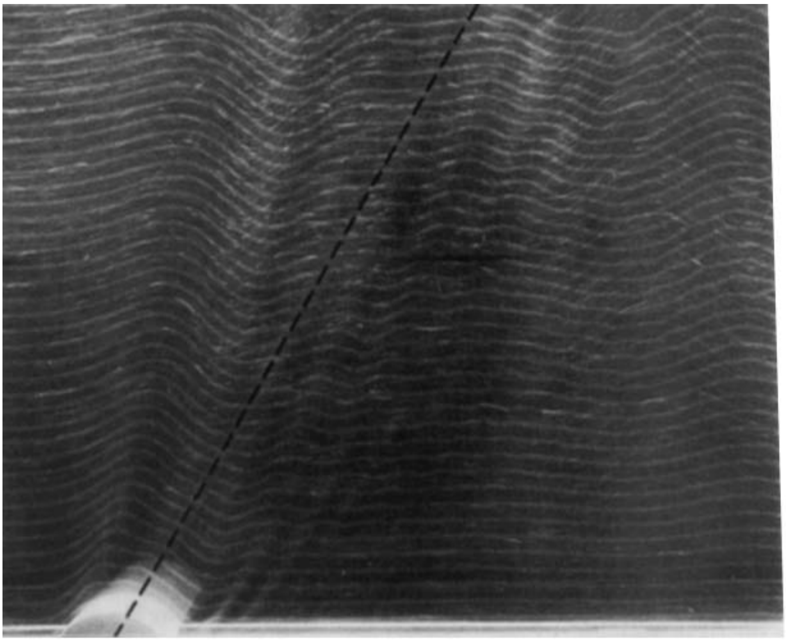

(*c*)

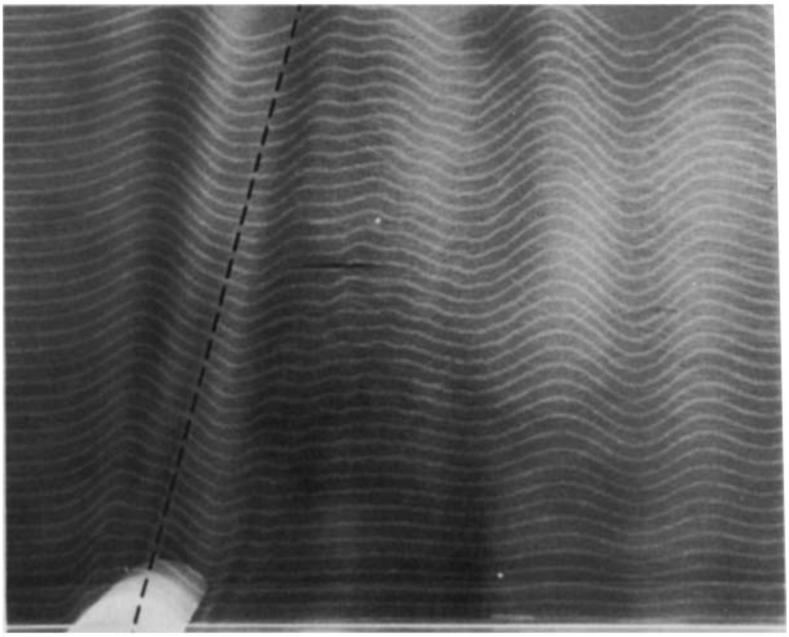

(*d*)

FIGURE 4. Flow over a cylindrical ridge $f_1(x)$ in the centreplane. Calculated streamlines are denoted by solid curves and group paths for $k_x = 4{\cdot}20$ are denoted by dashed lines. The top of the photograph is at $z = 0{\cdot}43$. In each case $L = 3{\cdot}81$ cm, $D = 91{\cdot}4$ cm, $h = 2{\cdot}32$ cm. (*a*) $Ro = 0{\cdot}179$, $H = 4{\cdot}30$, $E = 3{\cdot}13 \times 10^{-4}$ ($U = 1{\cdot}37$ cm/s, $\Omega = 1{\cdot}00\ \mathrm{s}^{-1}$); (*b*) $Ro = 0{\cdot}121$, $H = 2{\cdot}91$, $E = 3{\cdot}13 \times 10^{-4}$ ($U = 0{\cdot}928$ cm/s, $\Omega = 1{\cdot}00\ \mathrm{s}^{-1}$); (*c*) $Ro = 0{\cdot}0636$, $H = 1{\cdot}53$, $E = 1{\cdot}56 \times 10^{-4}$ ($U = 0{\cdot}974$ cm/s, $\Omega = 2{\cdot}01\ \mathrm{s}^{-1}$); (*d*) $Ro = 0{\cdot}0310$, $H = 0{\cdot}743$, $E = 0{\cdot}785 \times 10^{-4}$ ($U = 0{\cdot}946$ cm/s, $\Omega = 4{\cdot}01\ \mathrm{s}^{-1}$).

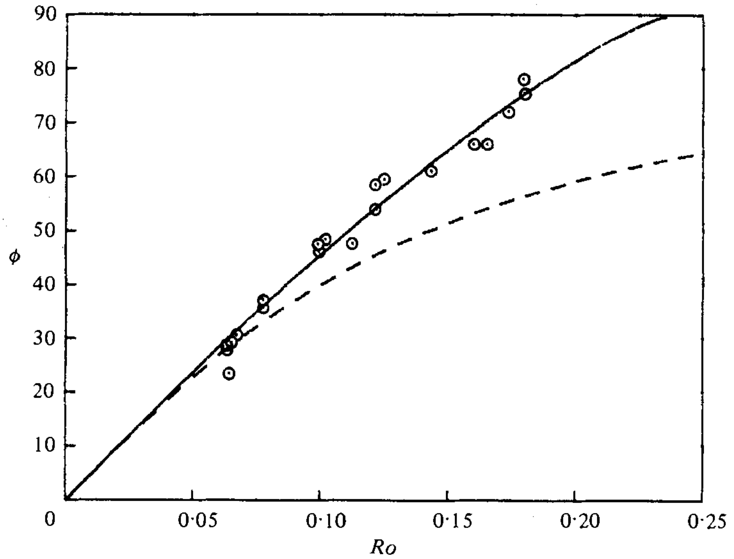

FIGURE 5. Group-path angle ϕ, for wavenumber $k_x = 4{\cdot}20$ versus *Ro* for flow over a cylindrical ridge. Observed values are denoted by circles. Calculated values are denoted by the solid line. The dashed line denotes the small-*Ro* limit.

comparison with experimentally observed waves generated by flow over a cylindrical ridge $f_1(x)$. This ridge matches the cylindrical ridge in height and volume displacement per unit length, and closely approximates it in shape. Figure 4 shows several such comparisons. Here the calculated streamlines are superimposed on photographs of waves. The ridge is towed from right to left. The top of the photograph is at a height about half the total depth of the fluid. The thickness of the light sheet illuminating the waves is about 0·6 cm at the top of the tank and 3 cm at the bottom.

The dashed lines in figure 4 are the group paths for $k_x = 4{\cdot}20$ according to (2.15), where, again, $k_x = 4{\cdot}20$ corresponds to the first zero in $F_1(k_x)$ for the cylindrical ridge. As discussed in §2, the amplitude of the vertical velocity is zero along this path, and, since the amplitude of the pressure perturbation is proportional to $|F_1(k_x)|$, it is also zero along this group path. To lowest order the horizontal velocity is zero along this path because the pressure serves as a stream function for the horizontal velocity. As a result, there are no waves along this path, and it is easily discernable from the surrounding regions containing waves. Figure 5 shows a comparison of the calculated group-path angle ϕ with measured values as a function of *Ro* for $k_x = 4{\cdot}20$. The dashed curve shows ϕ versus *Ro* for the small-*Ro* limit. The experimental data indicate that the small-*Ro* limit is not valid for $Ro > 0{\cdot}1$, in agreement with §2, where it was suggested that the vertical derivatives in the Laplacian would become important for $Ro > 0{\cdot}11$ for $k_x = 4{\cdot}20$.

The observed phase and amplitude correspond closely to that of the calculated streamlines near the first wave crest on the upstream side of the waves in figure 4. However, downstream from the first crest, the troughs and crests appear upstream of their calculated positions and observed amplitudes are much less than calculated. The observed amplitudes are expected to be less than the calculated values, since the calculations do not take viscosity into account. The damping appears to be greatest along the group paths for the highest wavenumbers in agreement with (2.7). The phase shift, except for the first crest, is particularly evident in the region occupied by the lower wavenumbers $k_x = 0$–$4{\cdot}20$, i.e. between the vertical axis and the dashed line.

The phase difference is less apparent in the region occupied by wavenumbers $k_x = 4{\cdot}20\text{–}Ro^{-1}$, i.e. between the dashed line and the horizontal plane. This is perhaps a nonlinear effect, since it is observed primarily for the largest-amplitude modes, those in the range $k_x = 0\text{–}4{\cdot}20$, although this does not explain why there is good agreement between observations and calculations in the vicinity of the first crest.

Another possible explanation for the discrepancy is that the sidewalls have not been taken into account in the calculations. The sidewalls block the cross-stream velocity v, and may cause the cross-stream horizontal flow to reverse direction sooner than it would if the sidewalls were not present. This would cause the first trough and subsequent crests and troughs to occur upstream of those calculated for strictly two-dimensional flow. The first crest would be less effected because it is upstream of the blocked cross-stream flow. The effect of the sidewalls is probably less evident for the region occupied by $k_x = 4{\cdot}20$ to Ro^{-1} because there the horizontal scale of these waves is small relative to the lateral dimension of the tank, and the flow is approximately two-dimensional.

Figure 6 compares the waves generated by flow over a cylindrical ridge with those generated by flow over a top-hat ridge for the same values of Ro, H and E. The group paths for the first and second zeros of $F(k_x)$ in each case are denoted by dashed lines. As discussed in §2, the amplitudes of the modes between these two group paths are generally larger for the top-hat ridge than for the cylindrical ridge. Although in figure 6 the photographs were obtained with short time exposures, and therefore do not show streaklines from which amplitudes can be measured, the degree of contrast between light and dark phase surfaces is indicative of the strength of shear, and suggests that larger amplitudes exist in this region for the top-hat ridge. Interestingly, the region between group-path angles $\phi = 0$ and 34·5° for the top-hat ridge is almost devoid of waves (figure 6*b*). A possible explanation may lie in the flow separation and turbulence visible near the ridge. It is clear that the flow near the ridge does not conform to the top-hat shape, and perhaps the large-scale features, which would be responsible for the missing part of the wave pattern, are lost owing to a change in the effective shape of the obstacle.

Figure 7 (*a*) shows waves generated by flow over a spherical cap $f_1(x, y)$, for the same values of Ro, H and E as in figure 6. The cross-sectional shape of the spherical cap in the centreplane is the same as that of the cylindrical ridge. However, the waves do not appear as intense for the spherical cap because the wave-energy density within the illuminated plane, which has finite thickness, is proportional to volume displaced by the obstacle within the illuminated plane, and the spherical cap displaces less volume than the cylindrical ridge within this region. Figure 7 (*b*), where the Ekman number E is twice as large as in figure 7 (*a*), shows the effect of viscous damping. Damping does not change the shape of the surfaces of constant phase, but reduces the amplitude of each mode in proportion to the square of its wavenumber. As a result the modes of highest wavenumber, i.e. the most horizontally propagating modes, have disappeared from the region $\phi = 60°\text{–}90°$ in figure 7 (*b*).

Figure 8 shows a comparison of the observed and calculated group path angles for the spherical cap. Here the group-path angle is for wavenumber $k_x = 4{\cdot}87$ and $k_y = 0$ corresponding to the first zero in $F_1(k_x, 0)$. The measured group-path angle is consistently less than that predicted by about 3° for $Ro = 0{\cdot}05$, increasing to about 7° for $Ro = 0{\cdot}15$. A possible explanation for the discrepancy is that the geostrophic component (§1), which has not been taken into account in the calculation of the group-path angle, has deflected the flow laterally on the downstream side of the obstacle. This deflection can be calculated assuming that potential vorticity is conserved in crossing the obstacle (Batchelor 1967) and is clearly evident when the

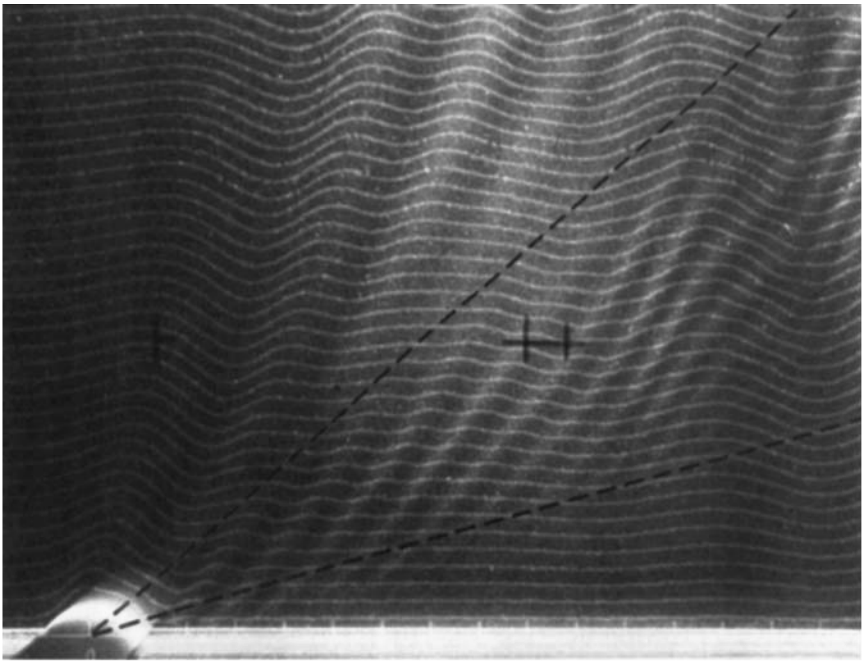

(a)

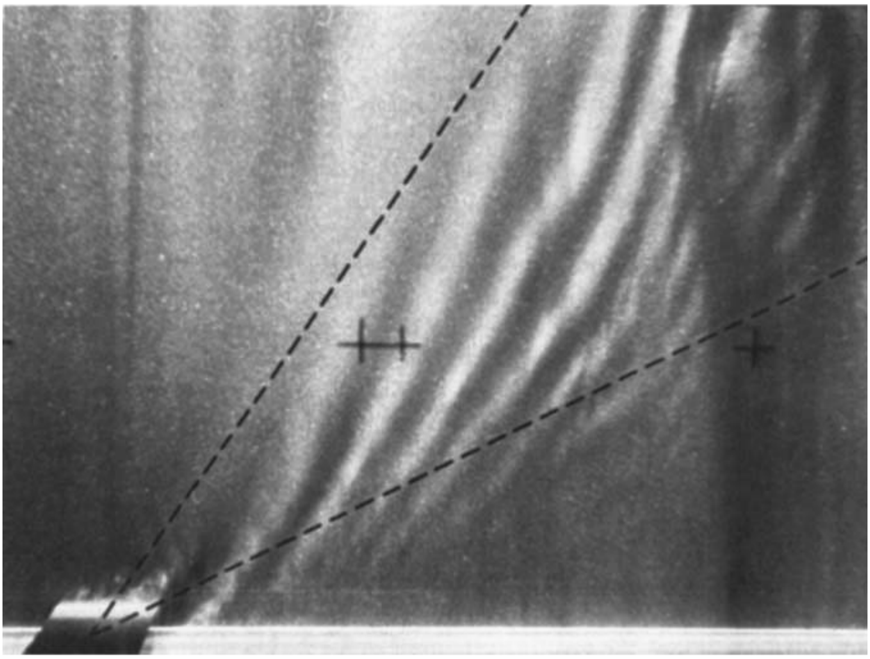

(b)

FIGURE 6. (a) Flow over a cylindrical ridge $f_1(x)$. (b) Flow over a top hat ridge $f_2(x)$. Dashed lines denote group paths for wavenumbers corresponding to the first and second zeros of $F(k_x)$. The top of each photograph is at $z = 0{\cdot}53$. $Ro = 0{\cdot}0987$, $H = 2{\cdot}37$, $E = 1{\cdot}36 \times 10^{-4}$ ($U = 1{\cdot}74$ cm/s, $L = 3{\cdot}8$ cm, $\Omega = 2{\cdot}31\ \mathrm{s}^{-1}$, $D = 91$ cm, $h = 2{\cdot}3$ cm).

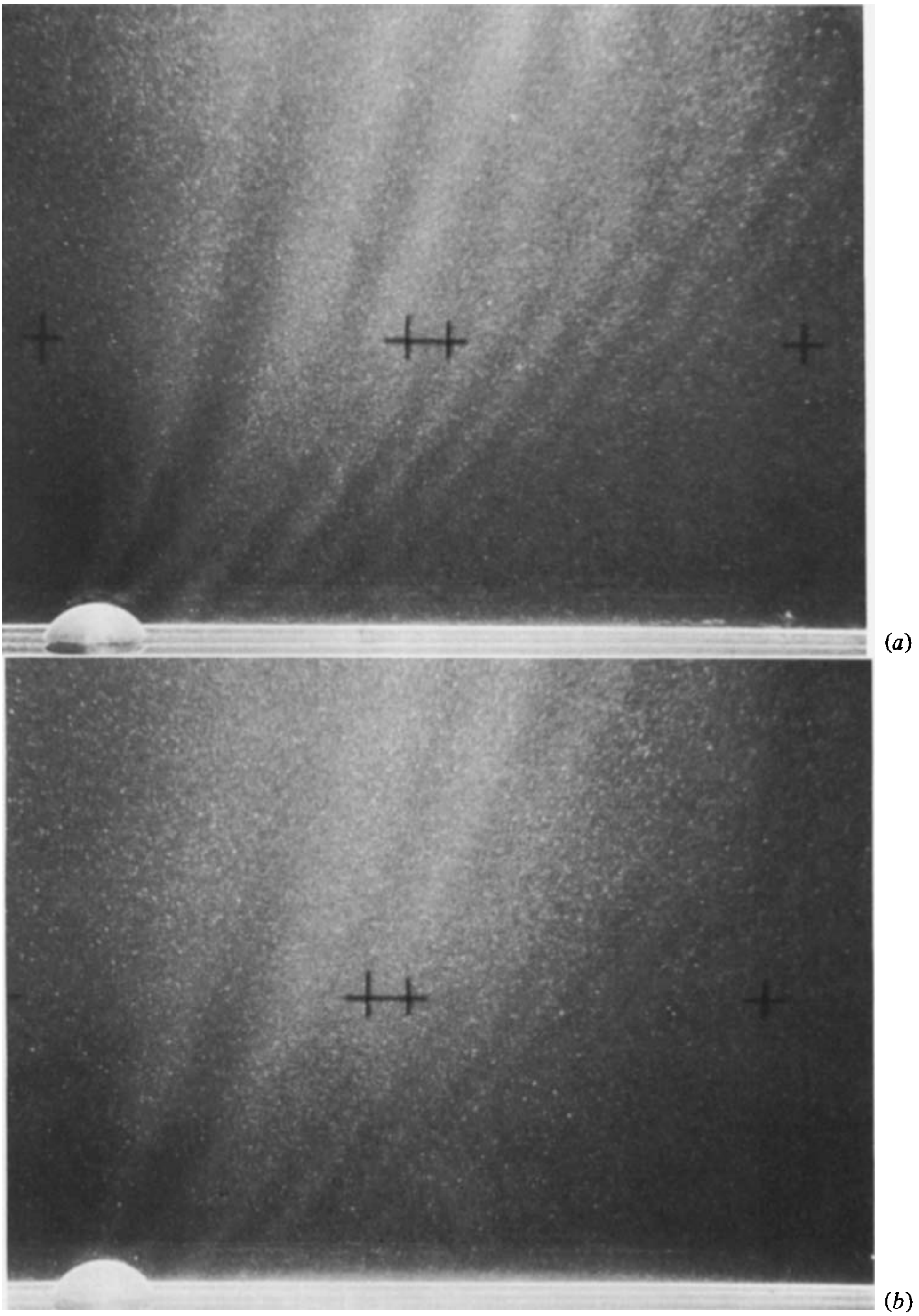

FIGURE 7. Flow over a spherical cap $f_1(r)$ in the plane $y = 0$. In (*b*) the value of E is twice that in (*a*), and increased viscous damping is evident. In each case $L = 3{\cdot}81$ cm, $D = 91{\cdot}4$ cm, $h = 2{\cdot}32$ cm. (*a*) $Ro = 0{\cdot}0996$, $H = 2{\cdot}39$, $HE = 1{\cdot}36 \times 10^{-4}$ ($U = 1{\cdot}76$ cm/s, $\Omega = 2{\cdot}21\ \mathrm{s}^{-1}$); (*b*) $Ro = 0{\cdot}0992$, $H = 2{\cdot}38$, $E = 2{\cdot}77 \times 10^{-4}$ ($U = 0{\cdot}858$ cm/s, $\Omega = 1{\cdot}14\ \mathrm{s}^{-1}$).

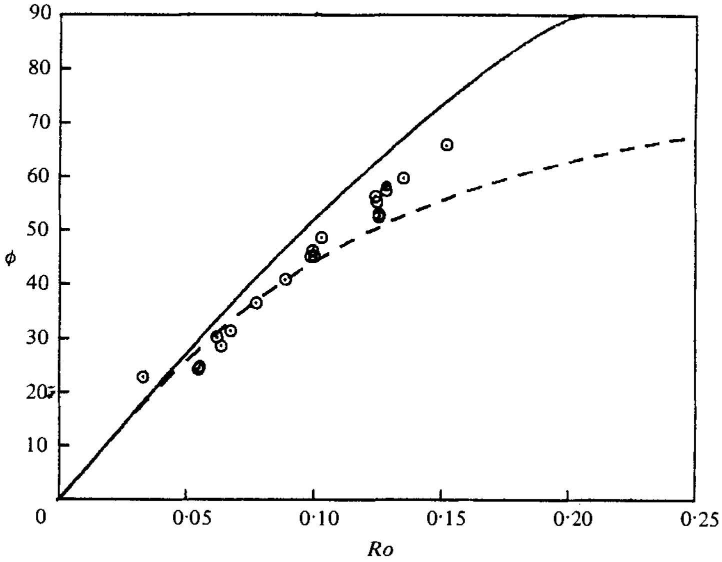

FIGURE 8. Group-path angle ϕ for wavenumber $(k_x, k_y) = (4{\cdot}87, 0)$ versus Ro for flow over a spherical cap. Observed values are denoted by circles. Calculated values are denoted by the solid line. The dashed line denotes the small-Ro limit.

waves are viewed in horizontal planes through the wave field (figures 10 and 12). The surfaces of constant phase are deflected with the mean flow, but otherwise seem to be undistorted. Thus the group-path angle measured in the centreplane $(k_y \neq 0)$, illuminated in the photographs, is not the same group-path angle calculated for the now deflected symmetry plane $(k_y = 0)$. The group-path angles for wavenumbers where $k_y = \text{constant} \neq 0$ corresponding to the first zero in $F_1(k_x, k_y)$ are less than that for $k_y = 0$, consistent with figure 8. The lateral walls counteract this deflection, and there is no net deflection of streamlines in the two-dimensional case (Huppert & Stern 1974), which explains why the discrepancy is not observed in figure 5. However, in the case of isolated obstacles relatively far from the walls, the flow may be deflected near the obstacle, and the influence of the lateral wall may only be apparent downstream from the region where the group-path angle is measured. Another possible explanation is that the nonlinear terms, not included in the calculations, are responsible for the discrepancy. As discussed in §2, nonlinearity is expected to be more important in the three-dimensional case. However, it is not clear that inclusion of the nonlinear terms would have the effect of lowering the calculated value of ϕ for a given Ro. Interestingly, the group-path angle calculated for the cylindrical ridge fits the spherical-cap data quite well.

Figure 9 shows the surfaces of constant phase in the plane $z^* = 5{\cdot}88h$ calculated from (2.15). The lower half shows the waves in the small-Ro limit. The full wave pattern in either case can be obtained by reflection through the centreplane. Note that the transverse and converging phase surfaces meet at the envelope of the wave pattern in a cusp, but had the next order in the stationary-phase approximation leading to (2.15) been included, there would be a phase shift of $\frac{1}{4}\pi$ at the caustic (Cheng 1977). There are several significant differences that arise in the small-Ro limit. First, in the small-Ro limit the caustic is a straight line inclined downstream at an angle of 19·5° from the centreplane rather than curving downstream from the vertex, and, secondly, the distance between neighbouring surfaces of constant phase is much less,

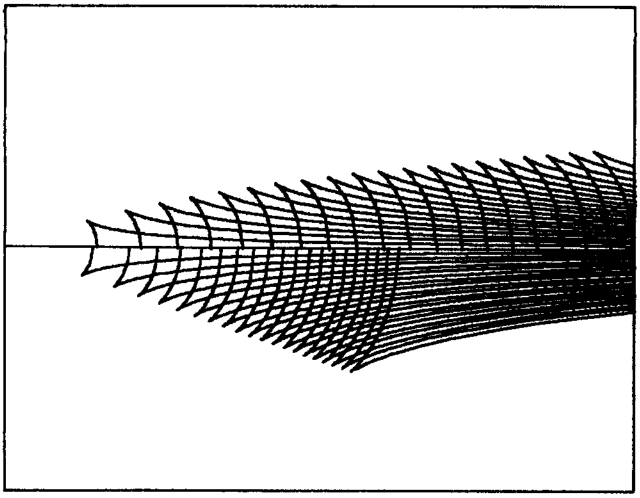

FIGURE 9. Surfaces of constant phase in the horizontal plane $z^* = 5{\cdot}88h$ for $Ro = 0{\cdot}122$ for full Ro-dependence (above) and small-Ro limit (below). In both cases the complete pattern is given by continuing the pattern by mirror symmetry to the opposite side of the centreplane.

owing to the phase surfaces curving upward more rapidly in the small-Ro limit. Another difference, not apparent in figure 9, is that the curvature of the caustic toward the downstream direction increases with increasing Ro and decreasing z.

Figure 10 shows a series of photographs, for decreasing Ro, of the flow over a spherical cap in same horizontal plane as the calculated phase surfaces in figure 9. The flow is viewed through a mirror beneath the tank, but is equivalent to the view from above with the direction of rotation counterclockwise. The obstacle is opaque and silhouetted against the light sheet illuminating the flow above. The width of the tank extends to the outer edges of the black borders. The sharp dark line at $y = 0$ is the towing wire. The diffuse dark line surrounded by two white lines, especially noticeable upstream of the obstacle, is the disturbance generated by the towing wire.

The decrease in the caustic wedge angle with increasing Ro and the curvature of the caustic at higher Ro are evident when figure 10(*a*) is compared with figure 10(*b*). Notice that the transverse waves are clear, but converging waves are not visible. They are expected to be weak because they correspond to the high-wavenumber low-amplitude waves, which are the most damped. However, it is surprising that they do not appear at all, at least near the obstacle where amplitudes are large. The asymmetry of the wave pattern about the centreplane is evident, particularly in figure 10(*b*). Figures 10(*b*, *c*) display a wide dark region extending from the right side of the photograph toward the obstacle. This feature is apparently associated with a low-velocity wake behind the obstacle, and is absent for $Ro > 0{\cdot}08$ (figure 10*a*). The strongest horizontal shear occurs on the left side (looking downstream) of the wake, and a series of shed cyclonic eddies appears on the right (figure 10*d*).

Figure 11 shows a series of photographs, for decreasing Ro, of the flow over a spherical cap in the centreplane for almost the same values of Ro as in figure 10. As Ro decreases, the surfaces of constant phase become straighter and more vertical. The group-path angle in the centreplane for the first zero-amplitude mode decreases, and the inertial waves become weaker. For small Ro, the surfaces of constant phase appear to form a column, tilting downstream from the obstacle (figure 11 *d*). This is the 'tilted Taylor column' observed by Hide *et al.* (1968). However, as H decreases further, a

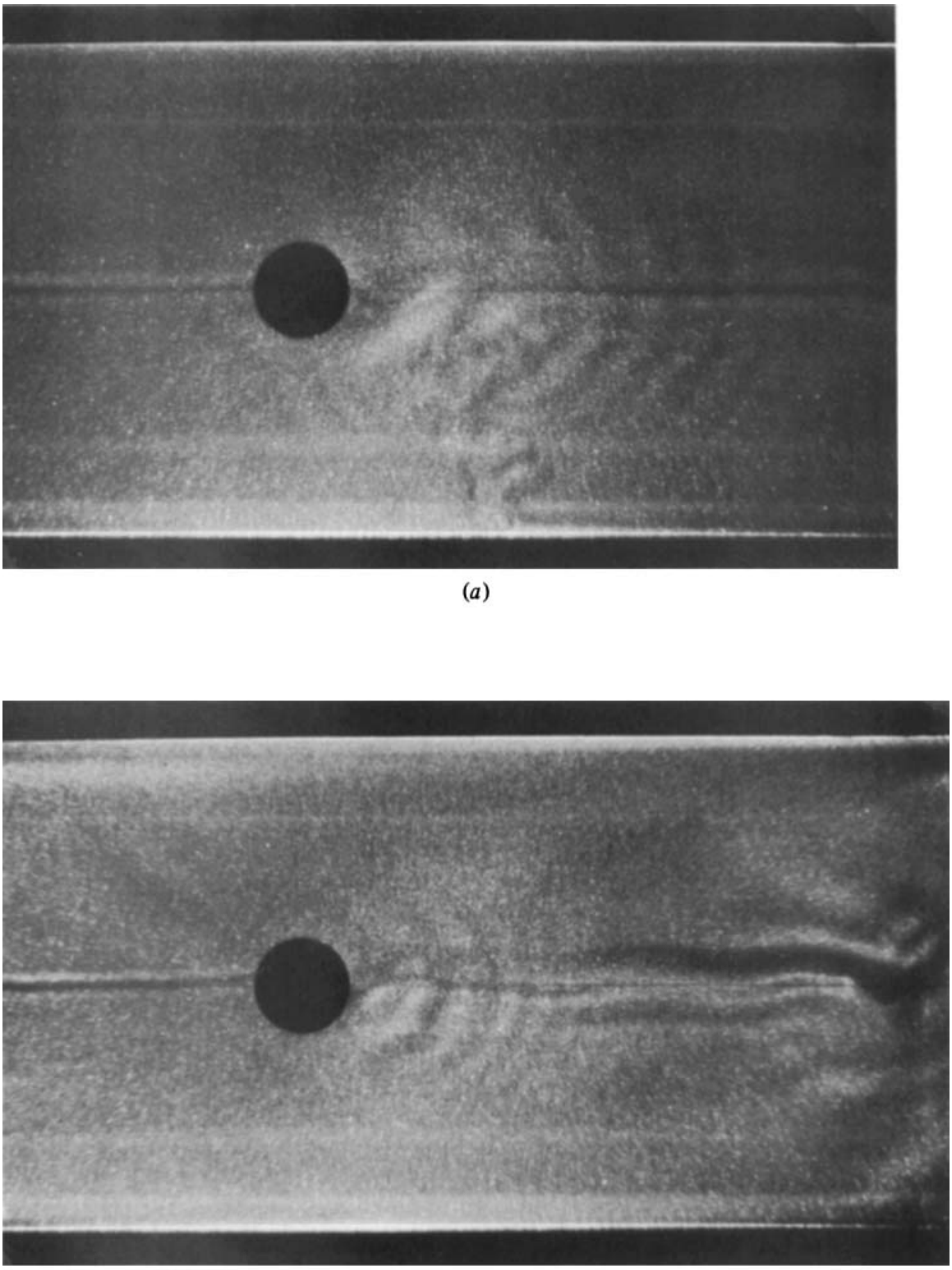

FIGURE 10(*a*, *b*). For caption see facing page.

columnar feature becomes visible that does not seem to be associated with the inertial waves. As H decreases, the strongly deflected flow above the obstacle gives rise to what appears to be a vertical free shear layer separating the oncoming flow, with velocity comparable to the free-stream velocity, from a low-velocity region above the obstacle (figure 12). The free shear layer first becomes visible in the upper half of the fluid, as indicated by the dashed lines in figures 11(*d*) and 13(*a*, *b*). It first becomes attached to the obstacle near the trailing edge and moves forward as H decreases.

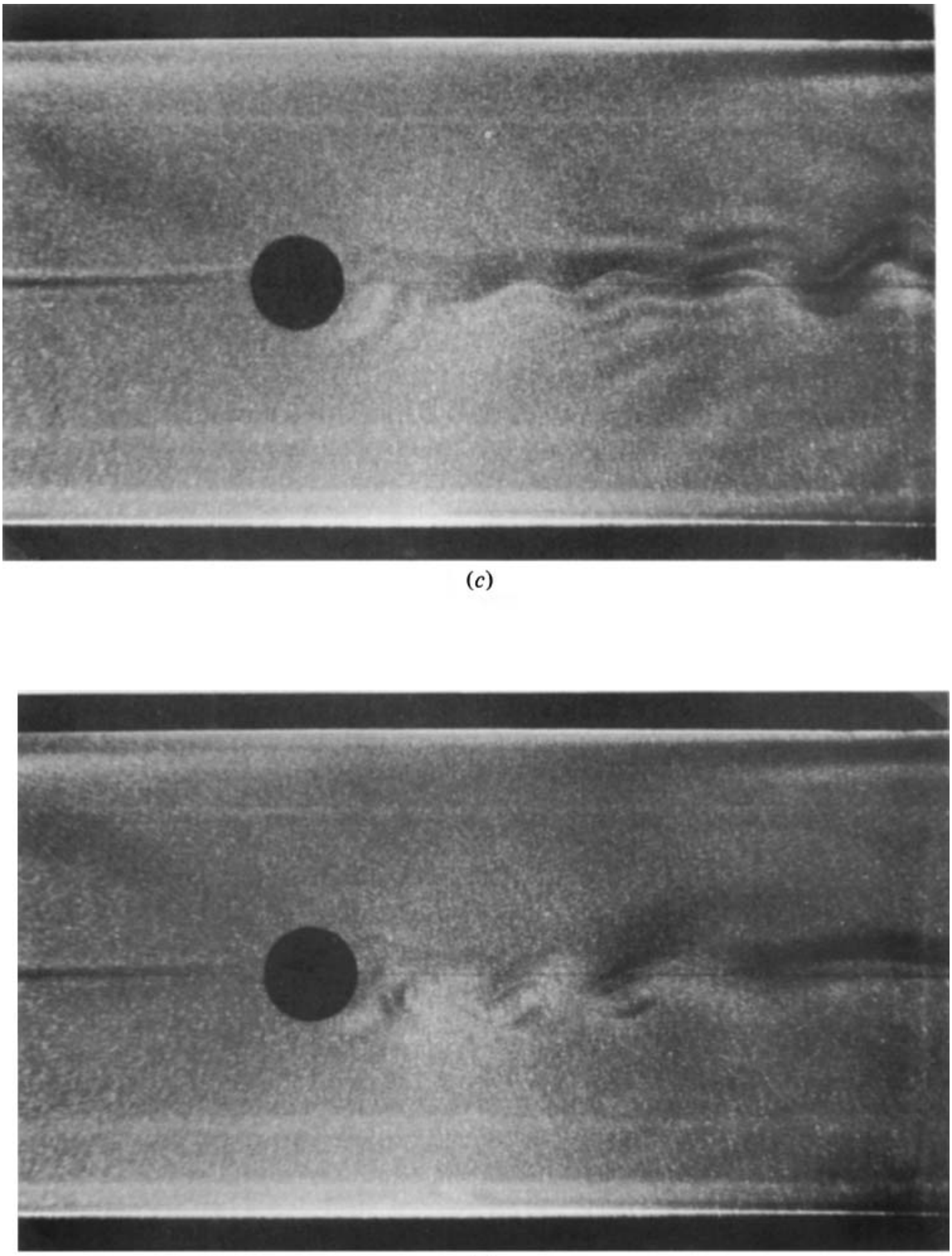
(*c*)

(*d*)

FIGURE 10. Flow over a spherical cap $f_1(r)$ in the horizontal plane $z^* = 5{\cdot}88h$. Direction of rotation is counterclockwise. Obstacle is traversing from right to left. In each case $L = 3{\cdot}81$ cm, $D = 91{\cdot}4$ cm, $h = 2{\cdot}32$ cm. (*a*) $Ro = 0{\cdot}122$, $H = 2{\cdot}93$, $E = 1{\cdot}36 \times 10^{-4}$ ($U = 2{\cdot}15$ cm/s, $\Omega = 2{\cdot}32\ \mathrm{s}^{-1}$); (*b*) $Ro = 0{\cdot}641$, $H = 1{\cdot}54$, $E = 0{\cdot}784 \times 10^{-4}$ ($U = 1{\cdot}96$ cm/s. $\Omega = 4{\cdot}02\ \mathrm{s}^{-1}$); (*c*) $Ro = 0{\cdot}0314$, $H = 0{\cdot}754$, $E = 0{\cdot}784 \times 10^{-4}$ ($U = 0{\cdot}961$ cm/s, $\Omega = 4{\cdot}02\ \mathrm{s}^{-1}$); (*d*) $Ro = 0{\cdot}0166$, $H = 0{\cdot}399$, $E = 0{\cdot}784 \times 10^{-4}$ ($U = 0{\cdot}509$ cm/s. $\Omega = 4{\cdot}02\ \mathrm{s}^{-1}$).

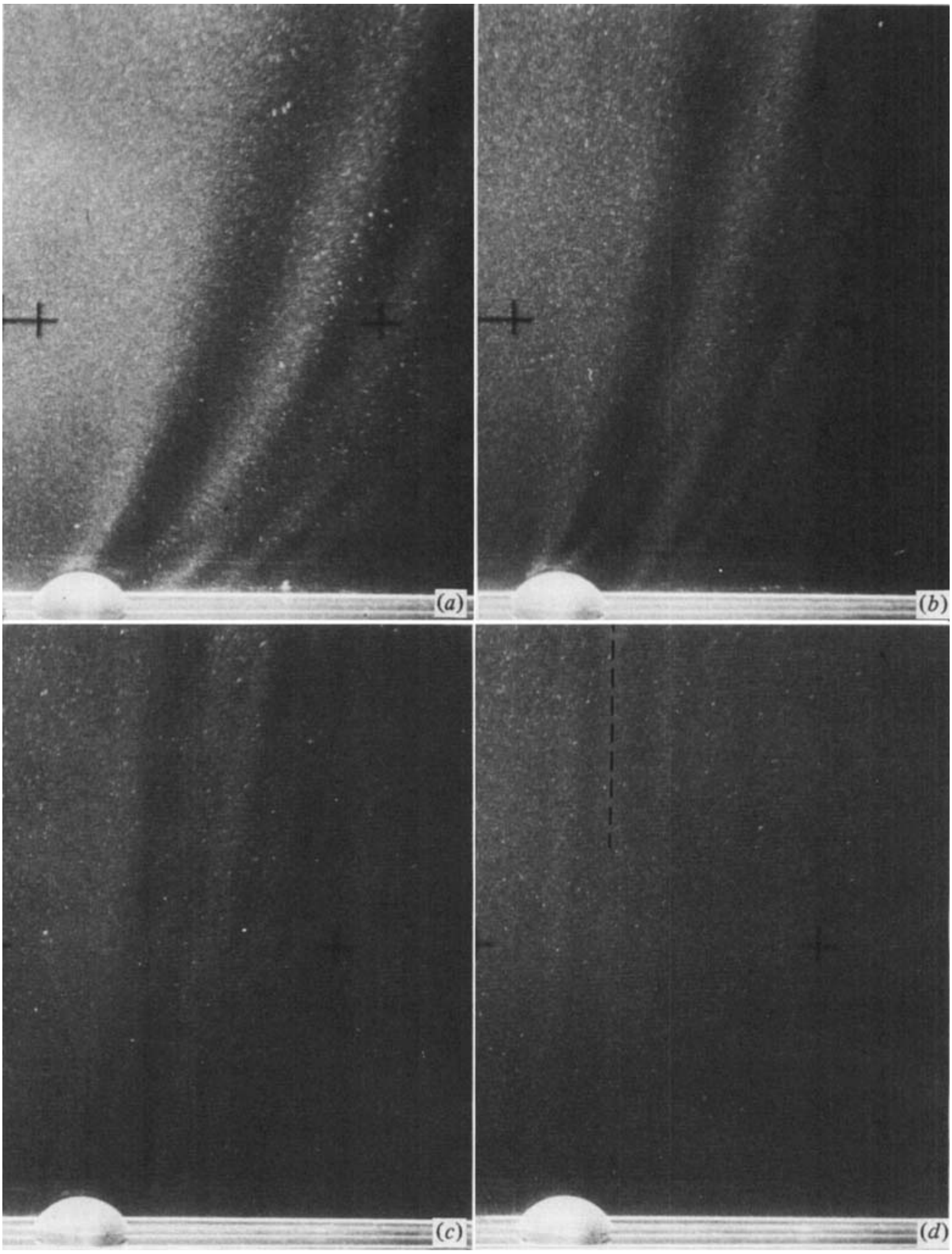

FIGURE 11. Flow over a spherical cap $f_1(r)$ in the plane $y = 0$. In each case $E = 1{\cdot}38 \times 10^{-4}$, $L = 3{\cdot}8$ cm, $\Omega = 2{\cdot}31\ \mathrm{s}^{-1}$, $D = 91{\cdot}4$ cm, $h = 2{\cdot}32$ cm. The top of the photograph is at $z = 0{\cdot}52$. (a) $Ro = 0{\cdot}123$, $H = 2{\cdot}96$ ($U = 2{\cdot}17$ cm/s); (b) $Ro = 0{\cdot}0673$, $H = 1{\cdot}61$ ($U = 1{\cdot}19$ cm/s); (c) $Ro = 0{\cdot}0329$, $H = 0{\cdot}788$ ($U = 0{\cdot}67$ cm/s); (d) $Ro = 0{\cdot}00887$, $H = 0{\cdot}213$ ($U = 0{\cdot}18$ cm/s).

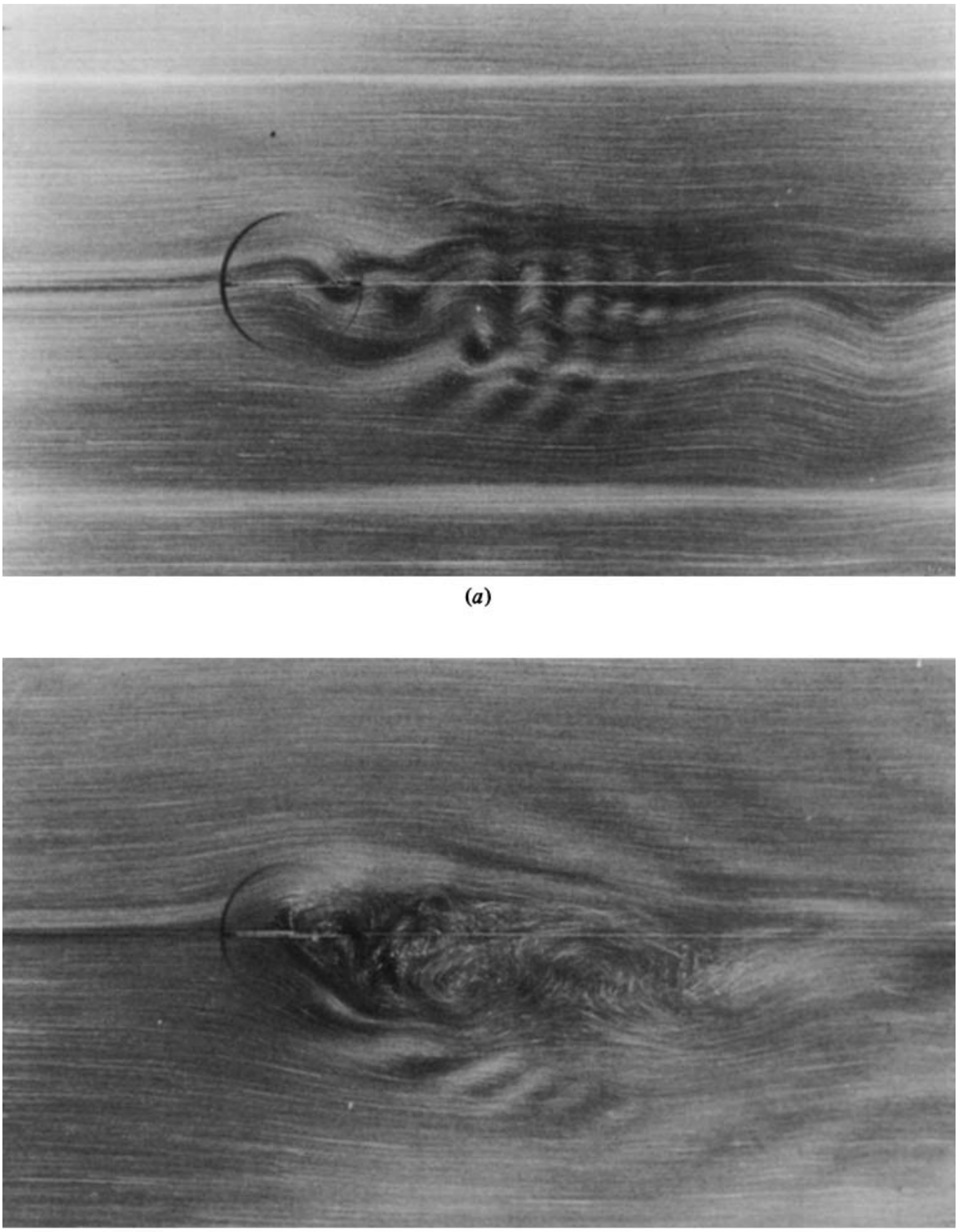

(*a*)

(*b*)

FIGURE 12. Flow over a right-circular cylinder $f_2(r)$ in the horizontal plane $z^* = 5{\cdot}35h$. The depth in (*b*) is one quarter that in (*a*). Time exposure ($\Delta t = U/L$) in the reference frame of the moving obstacle. Direction of rotation is counterclockwise. In both cases $E = 0{\cdot}861 \times 10^{-4}$, $L = 3{\cdot}81$ cm, $\Omega = 4{\cdot}00\ \mathrm{s}^{-1}$ and $h = 2{\cdot}41$ cm. (*a*) $Ro = 0{\cdot}0622$, $H = 1{\cdot}49$ ($U = 1{\cdot}89$ cm/s, $D = 91{\cdot}4$ cm); (*b*) $Ro = 0{\cdot}0625$, $H = 0{\cdot}375$ ($U = 0{\cdot}91$ cm/s, $d = 22{\cdot}9$ cm).

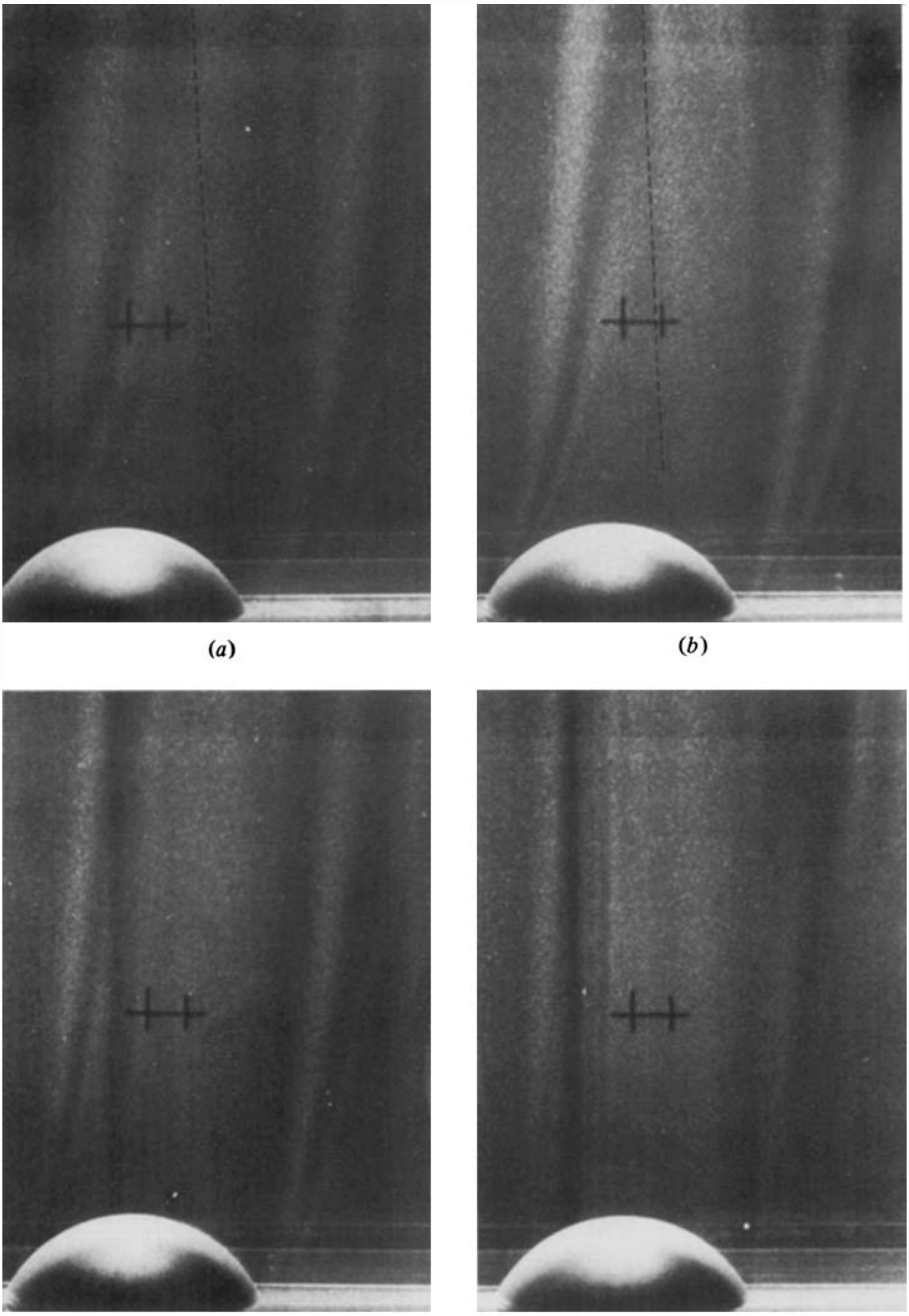

(a) (b) (c) (d)

FIGURE 13(a, b, c, d). For caption see facing page.

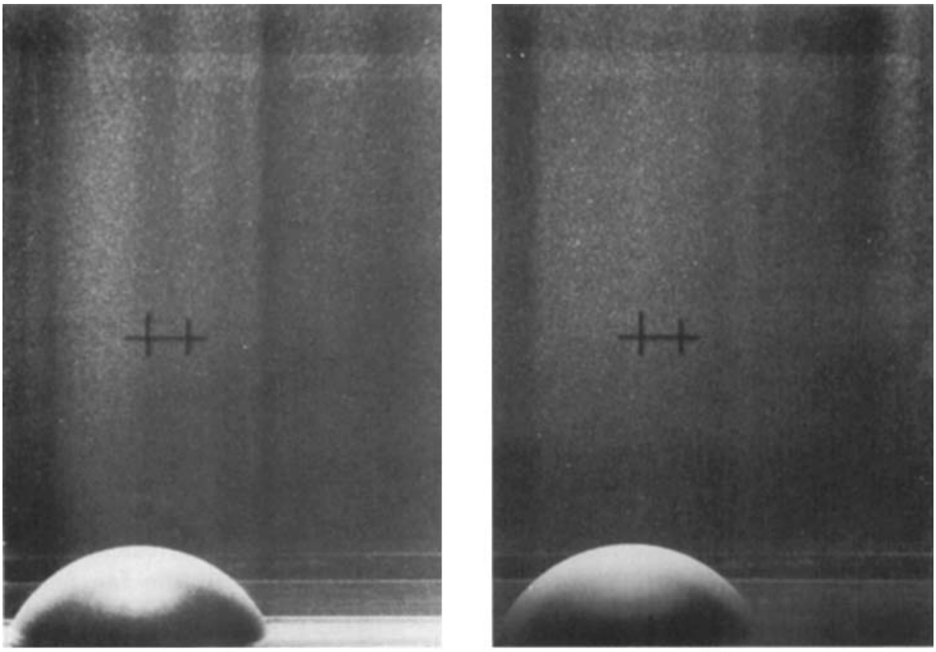

(*e*) (*f*)

FIGURE 13. Flow over a spherical cap $f_1(r)$ in the plane $y = 0$. The top of the photograph is at $z = 0{\cdot}52$. In each case $E = 0{\cdot}111\times10^{-4}$ ($L = 10{\cdot}2$ cm, $\Omega = 4{\cdot}01\ \mathrm{s}^{-1}$, $D = 91{\cdot}4$ cm, $h = 6{\cdot}19$ cm). (*a*) $Ro = 0{\cdot}0240$, $H = 0{\cdot}216$ ($U = 1{\cdot}95$ cm/s); (*b*) $Ro = 0{\cdot}0178$, $H = 0{\cdot}160$ ($U = 1{\cdot}44$ cm/s); (*c*) $Ro = 0{\cdot}0140$, $H = 0{\cdot}126$ ($U = 1{\cdot}14$ cm/s); (*d*) $o = 0{\cdot}0093$, $= 0{\cdot}0838$ ($U = 0{\cdot}758$ cm/s); (*e*) $Ro = 0{\cdot}00329$, $H = 0{\cdot}0296$ ($U = 0{\cdot}270$ cm/s); (*f*) $Ro = 0{\cdot}00150$, $H = 0{\cdot}0135$ ($U = 0{\cdot}122$ cm/s).

Inertial waves from the leading edge of the obstacle are either blocked or absorbed by this layer. For low Reynolds numbers $Re = Ro/E$, flow around the shear layer remains attached and inertial waves reappear at the trailing edge (figure 12). Fluid flows very slowly through shear layer and the region above the obstacle behind the shear layer, but does not appear to become trapped there for $H > 0{\cdot}001$. For higher Re, the critical value depending on obstacle shape and H, separation occurs at the shear layer, and vorticity is shed from the trailing side. Blocking by the shear layer results in a low-velocity wake downstream (figures 10 (*b*–*d*) and 12 (*b*)). In this case the wake rather than the obstacle may be the primary source of inertial waves (figure 12*b*). Unlike separation from a solid cylinder in a non-rotating fluid, eddy shedding only occurs on the right side of the shear layer, and the shed vorticity is of cyclonic sign in a system rotating counterclockwise about the z-axis, in agreement with Johnson (1978), for $Re < 3000$. Separation begins for $Re \approx 10^3$, several orders of magnitude larger than for a solid cylinder in the non-rotating case, in agreement with the observations of Boyer (1970).

We have tested the dependence of H_c, the value of H for the formation of the vertical free shear layer, on obstacle shape for $\epsilon = 0{\cdot}61$. Here H_c probably depends on Ro and E as well, but this dependence was not tested. The critical values are observed to be $H_c = 1{\cdot}0$ for the truncated right-circular cylinder and $H_c = 0{\cdot}2$ for the spherical cap. The effect of obstacle shape in the formation of closed streamlines above the obstacle has been considered by Huppert (1975) and Johnson (1978). Johnson (1978) shows that closed streamlines form over a truncated right-circular cylinder for

$H_c \approx \frac{1}{2}\epsilon$, and that H_c is less for a smoother obstacle, in qualitative agreement with our observations for the formation of the free shear layer. Further experiments are planned to examine the low-H case.

5. Conclusions

In this paper we have discussed the inertial waves formed by flow over ridges and isolated axisymmetric obstacles in a rotating fluid, and briefly discussed the transformation that takes place as H/ϵ decreases. For $H/\epsilon \gg 1$, inertial waves are the predominant feature; for $H/\epsilon \ll 1$ the vertical free shear layer is predominant.

Two-dimensional series solutions for the vertical velocity due to flow over ridges of shape $f(x) = 1 + a_2 x^2 + a_4 x^4$ in a fluid of finite depth have been found. These solutions have been used to calculate streamlines for comparison with experimental observations of flow over ridges. The phase and amplitude of the calculated streamlines agree reasonably well with the observations. Discrepancies noted are probably due to the lateral walls and viscosity, which have not been taken into account in the calculations.

Group-path angles and surfaces of constant phase have been calculated using Lighthill's asymptotic theory for linear dispersive waves in the far field, and comparisons have been made with the observed inertial waves. The agreement with experimental results is encouraging, particularly in view of the fact that the theory is not necessarily applied to the far field. A discrepancy in the group-path angle for the spherical cap may be due to the experimentally observed lateral deflection of the mean flow in the lee of the isolated obstacle, which has not been taken into account in the calculations.

The *Ro*-dependence of the shape of the caustic calculated for a point source is qualitatively the same as that observed for flow over a spherical cap. However, the converging family of phase surfaces is inexplicably absent. Similar calculations (streamlines, group paths and surfaces of constant phase) carried out for the small-*Ro* limit ($Ro \rightarrow 0$, H fixed) depart significantly from observations. The main problem with the small-*Ro* limit is that it does not account correctly for the contribution by the high wavenumbers. Moreover, the fundamental high-wavenumber cutoff is neglected entirely.

The formation of a tilted columnar disturbance by the inertial waves is observed for low *Ro*, but it is argued that this should not be interpretted as a Taylor column because (i) the column is not invariant along lines parallel to its axis, and (ii) it is not asymmetric about the centreplane. Furthermore, a vertical free shear layer separating the oncoming flow, with velocity comparable to the free-stream velocity, from a low-velocity, nearly stagnant region behind it is present for small H, which might more properly be construed as a Taylor column.

The authors would like to acknowledge the interest expressed by, and many helpful discussion with, H.-K Cheng during the course of this work. This work was supported by NSF grant CME-7822075.

REFERENCES

Batchelor, G. K. 1967 *An Introduction to Fluid Mechanics*, p. 574. Cambridge University Press.

Boyer, D. L. 1970 Flow past a right circular cylinder in a rotating frame. *Trans. A.S.M.E.* D: *J. Basic Engng* **92**, 430–436.

Cheng, H. K. 1977 On inertial wave and flow structure at low Rossby number. *Z. angew. Math. Phys.* **28**, 753–770.

Cheng, H. K. & Johnson, E. R. 1982 Inertial waves above topography in a unbounded, rapidly rotating fluid. *Proc. R. Soc. Lond.* A (to appear).

Greenspan, H. P. 1969 *The Theory of Rotating Fluids*. Cambridge University Press.

Hide, R. 1961 Origin of Jupiter's Great Red Spot. *Nature* **190**, 895–896.

Hide, R., Ibbetson, A. & Lighthill, M. J. 1968 On slow transverse flow past obstacles in a rapidly rotating fluid. *J. Fluid Mech.* **32**, 251–272.

Huppert, H. E. 1975 Some remarks on the initiation of inertial Taylor columns. *J. Fluid Mech.* **67**, 397–412.

Huppert, H. E. & Stern, M. E. 1974 The effect of side walls on homogeneous rotating flow over two-dimensional obstacles. *J. Fluid Mech.* **62**, 417–436.

Ingersoll, A. P. 1969 Inertial Taylor columns and Jupiter's Great Red Spot. *J. Atmos. Sci.* **26**, 744–752.

Jacobs, S. J. 1964 The Taylor column problem. *J. Fluid Mech.* **20**, 581–591.

Johnson, E. R. 1978 Trapped vortices in rotating flow. *J. Fluid Mech.* **86**, 209–224.

Johnson, E. R. 1982 The effects of obstacle shape and viscosity in deep rotating flow over finite-height topography. *J. Fluid Mech.* **120**, 359–383.

Lighthill, M. J. 1960 Studies on magnetohydrodynamic waves and anisotropic wave motions. *Phil. Trans. R. Soc. Lond.* A **252**, 397–430.

Lighthill, M. J. 1965 Group velocity. *J. Inst. Math. Appl.* **1**, 1–28.

Lighthill, M. J. 1967 On waves generated in dispersive systems by travelling forcing effects, with applications to the dynamics of rotating fluids. *J. Fluid Mech.* **27**, 725–752.

Lighthill, M. J. 1970 The theory of trailing Taylor columns. *Proc. Camb. Phil. Soc.* **68**, 485–491.

Lighthill, M. J. 1978 *Waves in Fluids*, pp. 254–255, 359. Cambridge University Press.

Mason, P. J. & Sykes, R. I. 1980 A numerical study of rapidly-rotating flow over surface-mounted obstacles. *J. Fluid Mech.* **111**, 175–196.

Maxworthy, T. 1971 A simple observational technique for the investigation of boundary-layers, stability and turbulence. In *Turbulence Measurements in Liquids* (ed. G. K. Paterson and J. L. Zakin). Dept Chem. Engng, Univ. Missouri: Rolla.

Proudman, J. 1916 On the motion of solids in a liquid possessing vorticity. *Proc. R. Soc. Lond.* A **92**, 408–424.

Stewartson, K. & Cheng, H. K. 1979 On the structure of inertial waves produced by an obstacle in a deep rotating container. *J. Fluid Mech.* **91**, 415–432.

Taylor, G. I. 1917 Motion of solids in fluids when the flow is not irrotational. *Proc. R. Soc. Lond.* A **93**, 99–113.

Taylor, G. I. 1923 Experiments on the motion of solids in rotating fluids. *Proc. R. Soc. Lond.* A **104**, 213–218.